Supporting Information Appendix for: "Superconductivity and non-Fermi liquid behavior near a nematic quantum critical point"

Samuel Lederer,[1,*] Yoni Schattner,[2,*] Erez Berg,[2] and Steven A. Kivelson[3]

[1] *Department of Physics, Massachusetts Institute of Technology, Cambridge, MA 02139, USA*
[2] *Department of Condensed Matter Physics, The Weizmann Institute of Science, Rehovot, 76100, Israel*
[3] *Department of Physics, Stanford University, Stanford, CA 94305, USA*

The nematic phase boundary has been determined using standard finite size scaling techniques appropriate to a two-dimensional classical Ising transition, as described in the appendix of Ref. 1. The superconducting transition temperature has been determined using the helicity modulus, following Ref. 2:

$$\rho_s = \lim_{q_y \to 0} \lim_{L \to \infty} K_{xx}(q_x = 0, q_y) \tag{S1}$$

where

$$K_{xx}(\mathbf{q}) \equiv \frac{1}{4} \left[\Lambda_{xx}(q_x \to 0, q_y = 0) - \Lambda_{xx}(\mathbf{q}) \right], \tag{S2}$$

and Λ_{xx} is the current-current correlator

$$\Lambda_{xx}(\mathbf{q}) = \sum_i \int_0^\beta d\tau e^{-i\mathbf{q}\cdot\mathbf{r}_i} \langle J_x(\mathbf{r}_i, \tau) J_x(0,0) \rangle. \tag{S3}$$

Here, the current density operator is given by $J_x(\mathbf{r}_i) = \sum_\sigma it(1 + \alpha\tau^z_{i,j}) c^\dagger_{i\sigma} c_{j\sigma} + \text{H.c.}$, where $\mathbf{r}_j = \mathbf{r}_i + \hat{x}$. The $q \to 0$ limits above are not strictly well defined for finite size systems, so we use the smallest nonzero momentum $q = 2\pi/L$ to define a value of ρ_s in finite size systems. Fig. S1 exhibits curves of $\rho_s(T)$ for various system sizes, which cross at a temperature near where they attain the BKT jump of $2T/\pi$. Rough error bars are determined by inspection.

The T_c determined above can be corroborated by examining other thermodynamic quantities (Fig.). For instance the pair susceptibility

$$P_s = \int_0^\beta d\tau \sum_i \langle \Delta^\dagger_s(\mathbf{r}_i, \tau) \Delta_s(0,0) \rangle. \tag{S4}$$

where, $\Delta_s(\mathbf{r}_i) = c_{i\uparrow} c_{i\downarrow}$ diverges in the thermodynamic limit only in the superconducting phase. The uniform spin susceptibility also shows evidence of the opening a spin gap in the superconducting phase.

---

* These authors have contributed equally to this work.

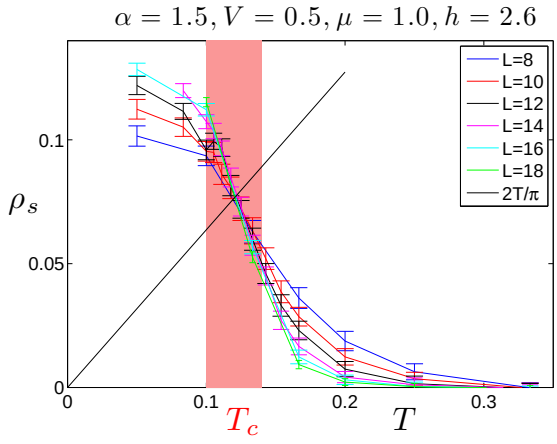

Figure S1. Helicity modulus versus temperature for various system sizes. The black line represents the BKT jump of $2T/\pi$.

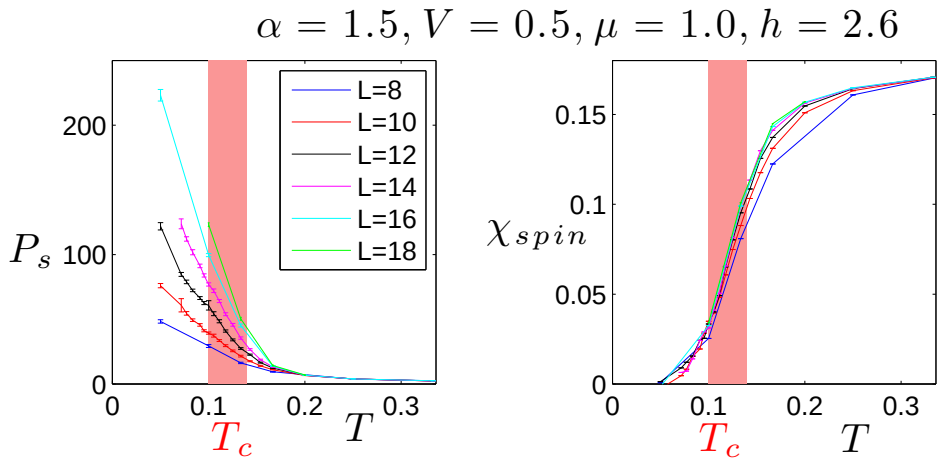

Figure S2. Left: the onset s-wave pairing susceptibility versus temperature. Right: the uniform spin susceptibility versus temperature. Both are shown for various system sizes, and indicate a superconducting T_c consistent with that determined above.

S-I. ESTIMATING THE DC RESISITIVITY

A. Resistivity proxy from the long imaginary time data

Next, we describe the "resistivity proxy" ρ_2 introduced in the main text as an estimator for the d.c. resistivity, $\rho_{\rm dc}$. ρ_2 can be computed directly from imaginary time data (without the need for any

analytical continuation). It is proportional to $\rho_{\rm dc}$ under certain assumptions, as we discuss below. We have used the resistivity proxy analysis as a complement to direct analytical continuation. The fact that both approaches give a qualitatively similar temperature dependence for the resistivity, and even the quantitative estimates agree within a factor of ~ 2 (see Fig. 5 of the main text), provides support for the validity of our assumptions.

The imaginary-time (and Matsubara frequency) current-current correlations are related to the real part of the real-frequency conductivity by

$$\Lambda(i\omega_n) = \int \frac{d\omega}{\pi} \frac{\omega^2 \sigma'(\omega)}{\omega^2 + \omega_n^2}. \tag{S5}$$

$$\tilde{\Lambda}(\tau) = \int \frac{d\omega}{2\pi} \sigma'(\omega) \frac{\omega \cosh\left[(\frac{\beta}{2} - \tau)\omega\right]}{\sinh\left(\frac{\beta\omega}{2}\right)}, \tag{S6}$$

[Note that Eq. (S6) is valid for $0 \leq \tau \leq \beta$.] Since the kernels in Eqs. (S6,S5) are ill-conditioned, inverting these equations is a highly numerically unstable problem. To make matters worse, $\sigma'(\omega)$ turns out to have features whose characteristic width is of order T or less - which is less than the intrinsic "resolution" of the kernel.

However, under many circumstances, we would expect that $\sigma'(\omega, T)$ at low frequencies is determined by the behavior of $\tilde{\Lambda}(\tau)$ at the longest imaginary times, $\tau \sim \beta/2$, or equivalently by the low-frequency moments (LFMs) [3]

$$m_0 \equiv \beta \widetilde{\Lambda}(\tau = \frac{\beta}{2}) = \beta \int \frac{d\omega}{2\pi} \frac{\omega \sigma'(\omega)}{\sinh\left(\frac{\beta\omega}{2}\right)}, \tag{S7}$$

$$m_2 \equiv \beta \partial_\tau^2 \widetilde{\Lambda}(\tau = \frac{\beta}{2}) = \beta \int \frac{d\omega}{2\pi} \frac{\omega^3 \sigma'(\omega)}{\sinh\left(\frac{\beta\omega}{2}\right)}, \tag{S8}$$

in terms of which the resistivity proxy defined in the text is

$$\rho_2 \equiv \frac{m_2}{2\pi T m_0^2} = \left. \frac{\partial_\tau^2 \widetilde{\Lambda}}{2\pi \widetilde{\Lambda}^2} \right|_{\tau = \beta/2} \tag{S9}$$

To illustrate the usefulness of this definition, consider the simple case in which $\sigma'(\omega)$ is a Lorentzian,

$$\sigma'(\omega, T) = \frac{1}{\rho} \left[\frac{\Gamma^2}{\omega^2 + \Gamma^2} \right] \quad \rightarrow \quad \frac{\rho_2}{\rho} = \frac{2\pi^2 - \beta\Gamma F(\beta\Gamma)}{[F(\beta\Gamma)]^2} \tag{S10}$$

where

$$F(x) = 2x \left[\psi\left(\frac{x}{2\pi}\right) - \psi\left(\frac{x}{4\pi}\right) - \log(2) \right] - 2\pi, \tag{S11}$$

and $\psi(x)$ is the digamma function. It is easy to see that ρ_2/ρ does not depend very strongly on $\beta\Gamma$. Specifically, $\rho_2 \to \rho$ as $\beta\Gamma \to \infty$ and $\rho_2 \to \rho/2$ as $\beta\Gamma \to 0$ (*i.e.* for a narrow Lorentzian).

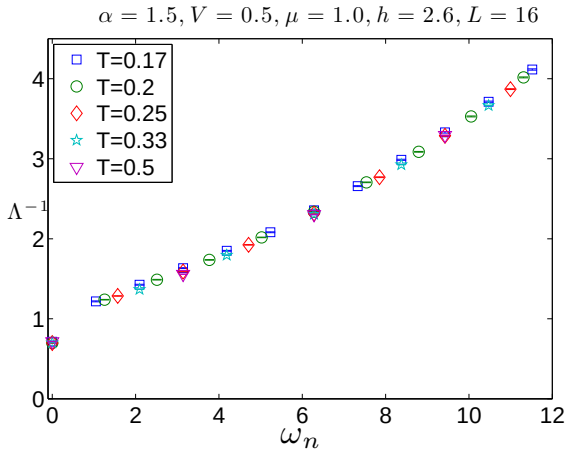

Figure S3. $\Lambda^{-1}(i\omega_n)$ at $h \approx h_c$ for different temperatures. The parameters used in the runs are $\alpha = 1.5$, $V = 0.5$, $\mu = -1$, and $h = 2.6$.

Naturally, especially at criticality, it is not reasonable to expect $\sigma'(\omega)$ to have a simple Lorentzian form. However, ρ_2 turns out to provide a reasonable estimate of ρ under much more general circumstances. Specifically, let us assume that

$$\sigma'(\omega, T) = \sigma_D(\omega, T) + \sigma_{\rm reg}(\omega, T), \tag{S12}$$

where $\sigma_D(\omega, T)$ is a Drude-like piece (*i.e.* maximal at $\omega = 0$), that satisfies

$$\sigma_D(\omega, T) \xrightarrow[T\to 0]{} D\delta(\omega), \tag{S13}$$

and whose characteristic width at finite temperature is of the order of T or less, while $\sigma_{\rm reg}(\omega, T)$ is a regular piece with a width that is always large compared to T and correspondingly a magnitude at low frequencies ($\omega \lesssim T$) that is small compared to σ_D (*i.e.* $\sigma'_D(0, T) \gg \sigma_{\rm reg}(0, T)$). Evidence for the validity of Eq. (S12) in our problem can be seen by comparing $\Lambda(i\omega_n)$ for different temperatures. This is shown in Fig. S3. For all temperatures, $\Lambda(i\omega_n)$ has an apparent "jump" from $\omega_n = 0$ to $\omega_n > 0$. $\Lambda(i\omega_n)$ for different temperatures are seen to approximately lie on a single, nearly temperature-independent curve. Both features can be readily understood from Eq. (S12). The jump at $\omega_n = 0$ is a consequence of $\sigma_D(\omega, T)$, which so long as its width is less than $2\pi T$ behaves effectively as if it were a delta function at $\omega_n = 0$. The fact that finite ω_n data from different temperatures lie on a single curve suggests that $\sigma_{\rm reg}(\omega, T)$ is not strongly T dependent over the relevant range of T.

We are now faced with the task of disentangling $\sigma_{\rm reg}(\omega)$ and $\sigma_D(\omega)$. The LFMs clearly combine information about both $\sigma_{\rm reg}$ and σ_D. Crucially, however, the two contributions *may scale differently with temperature as* $T \to 0$. Consider $\sigma_{\rm reg}$: its contribution to the LFMs, to lowest order in T, is

expected to behave as

$$m_{0,\mathrm{reg}} = \beta \int \frac{d\omega}{2\pi} \frac{\omega \left[\sigma_{\mathrm{reg}}(0) + \frac{1}{2}\partial_\omega^2 \sigma_{\mathrm{reg}}(0)\omega^2 + \dots\right]}{\sinh\left(\frac{\beta\omega}{2}\right)} \sim T + O(T^3),$$
$$m_{2,\mathrm{reg}} = \beta \int \frac{d\omega}{2\pi} \frac{\omega^3 \left[\sigma_{\mathrm{reg}}(0) + \frac{1}{2}\partial_\omega^2 \sigma_{\mathrm{reg}}(0)\omega^2 + \dots\right]}{\sinh\left(\frac{\beta\omega}{2}\right)} \sim T^3 + O(T^5). \tag{S14}$$

In contrast, assuming $\sigma_D(\omega)$ has a width of the order of T or less, its corresponding LFMs will scale differently. If the total weight of $\sigma_D(\omega)$ has a non-zero limit as $T \to 0$, and if the characteristic width of $\sigma_D(\omega)$ is much less than T, we expect

$$m_{0,D} = \beta \int \frac{d\omega}{2\pi} \frac{\omega \sigma_D(\omega)}{\sinh\left(\frac{\beta\omega}{2}\right)} \approx \int \frac{d\omega}{\pi} \sigma_D(\omega), \tag{S15}$$

and hence, this is non-zero in the $T \to 0$ limit. This is true also if the characteristic width of $\sigma_D(\omega)$ is of the order of T. For example, if σ_D has a scaling form: $\sigma_D(\omega, T) = \frac{1}{T} f\left(\frac{\omega}{T}\right)$, then we get that $m_{0,D} \to \int_{-\infty}^{\infty} dx \frac{x f(x)}{2\sinh\left(\frac{x}{2}\right)} = $ const. in the limit $T \to 0$. In our data, we find that over a range of temperatures, $m_0(T)$ is weakly temperature dependent, suggesting that it is dominated by $m_{0,D}$ (see Fig. S4).

The interpretation of m_2 is more subtle, as it depends on the precise form of $\sigma_D(\omega)$ at frequencies of the order of T. It is instructive to consider a simple model for $\sigma_D(\omega, T)$:

$$\sigma_D(\omega, T) = \begin{cases} \sigma_0(T), & \omega < \omega_0(T), \\ \sigma_0(T) \left(\frac{\omega}{\omega_0}\right)^{-\alpha}, & \omega_0(T) < \omega. \end{cases} \tag{S16}$$

with $\omega_0(T) < AT$, where A is a constant. Having a finite optical weight requires $\alpha > 1$. Then, to be consistent with the observation that $m_{0,D} \approx$ const., we require that $\sigma_0(T)\omega_0(T) = D = $ const. We then get that

$$\begin{aligned} m_{2,D} &\approx \sigma_0(T) \int_0^{\omega_0(T)} d\omega \omega^2 + \sigma_0 \int_{\omega_0(T)}^{T} d\omega \omega^2 \left(\frac{\omega}{\omega_0}\right)^{-\alpha} \\ &= \frac{1}{3} D\omega_0^2 + \frac{1}{3-\alpha} D\omega_0^2 \left[\left(\frac{T}{\omega_0}\right)^{3-\alpha} - 1\right]. \end{aligned} \tag{S17}$$

We see that, if $\omega_0/T \to 0$ as $T \to 0$, we get that $m_{2,D}/T^2 \to 0$ as $T \to 0$. For example, if $\omega_0 \sim T^{1+\varepsilon}$ with $\varepsilon > 0$, then $m_{2,D} \sim T^{\min[2+(\alpha-1)\varepsilon,\, 2(1+\varepsilon)]}$. On the other hand, if $\omega_0 \sim T$, we get that $m_{2,D} \sim T^2$.

As another example, one can analyze the low-frequency conductivity of a clean Fermi liquid with umklapp scattering. The conductivity is given by

$$\sigma_{\mathrm{FL}}(\omega) = \frac{D}{\pi} \frac{\Gamma_{\mathrm{tr}}(T, \omega)}{[\Gamma_{\mathrm{tr}}(T, \omega)]^2 + \omega^2}, \tag{S18}$$

where the Fermi liquid transport scattering rate is $\Gamma_{\mathrm{tr}}(T, \omega) = (\omega^2 + 4\pi^2 T^2)/W$ (W is of the order of the Fermi energy). The integral for m_0 can be calculated in the limit $T \to 0$, and gives $m_0 = D$. The integral for m_2 is dominated by frequencies $\omega \sim T$, such that at low temperatures, $m_2 \sim T^3$.

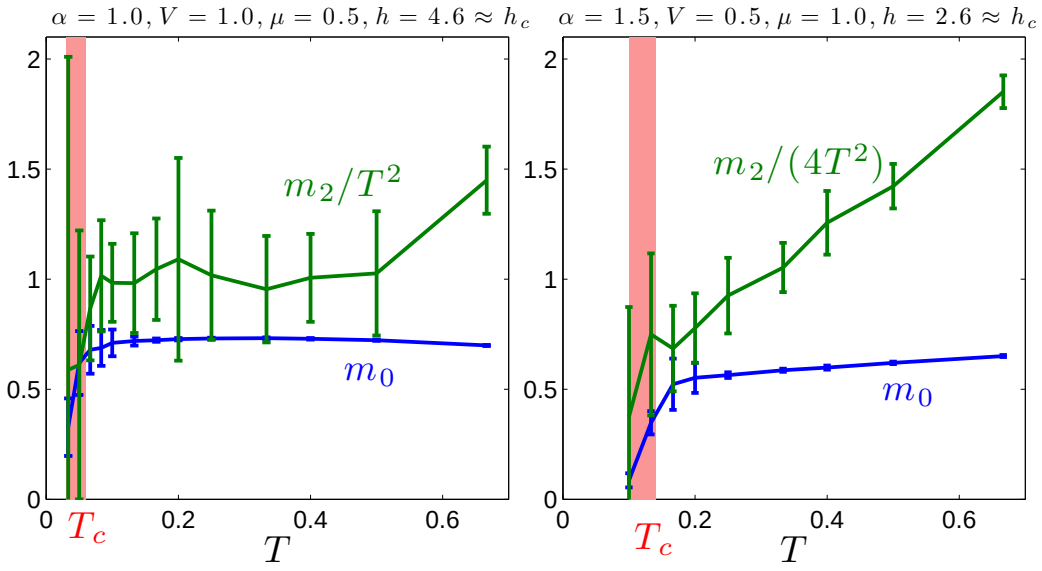

Figure S4. m_0 and m_2/T^2 as a function of T at criticality.

Turning to our DQMC data, m_0 and m_2 as a function of temperature at criticality are shown in Fig. S4 for two sets of parameters. We find that both m_0 and m_2/T^2 extrapolate to a non-zero value in the limit $T \to 0$. This implies that these moments are indeed dominated by the contribution of σ_D. For the larger T_c parameter set (right panel), both quantities show a sudden drop at temperatures below $T = 0.2t$; this is likely to be an effect of superconducting fluctuations upon approaching the superconducting critical temperature, $T_c \approx 0.11t$. Over a range of temperatures above $T = 0.05t$ (left panel) and $T = 0.2t$ (right panel), the observed behavior is consistent with $\omega_0 \propto T$ in Eq. (S16) and with $\sigma_0 \propto 1/T$.

It is worth noting that there are other possible ways to define a resistivity proxy in terms of m_0 and m_2, depending on the assumed form of σ at criticality. For instance, if $\sigma_D(\omega) = \sigma_0 g\left(\frac{\omega}{\Gamma}\right)$, where $g(x)$ is a dimensionless function with a well-defined second moment (unlike a Lorentzian) and $\Gamma \leq AT$, we get that $m_0 \propto \sigma_0 \Gamma$ and $m_2 \propto \sigma_0 \Gamma^3$. In this case, a more appropriate resistivity proxy is

$$\tilde{\rho}_2 = \frac{\sqrt{m_2/m_0}}{m_0} \propto \frac{1}{\sigma_0}. \tag{S19}$$

In the particular case where $\Gamma \propto T$, $\sigma_0 \propto 1/T$, both ρ_2 and $\tilde{\rho}_2$ are proportional to T. Reassuringly, computing $\tilde{\rho}_2$ from our DQMC data at criticality produces qualitatively similar results as ρ_2.

B. Fitting function for $\Lambda(\omega_n)$

In order to fit the imaginary-time data for the current-current correlator, $\Lambda(\omega_n)$, we use the following model for the optical conductivity [Eq. (4) of the main text]:

$$\Lambda_{\rm fit}(\omega_n) = \sum_{j=1}^{N} \frac{A_j}{\omega_n^2 + \gamma_j|\omega_n| + \Omega_j^2}, \tag{S20}$$

with free parameters A_j, γ_j, Ω_j, and we have found that $N = 2$ is sufficient to fit our data. When comparing this form to the QMC data, we need to recall that the QMC simulations are performed with a finite imaginary time step, $\Delta\tau$. The imaginary time correlation function $\widetilde{\Lambda}(\tau)$ is sampled at discrete values $\tau = n\Delta\tau$ (where n is an integer), and $\Lambda(\omega_n)$ is its discrete Fourier transform. In particular, $\Lambda(\omega_n)$ is periodic in ω_n with a period of $2\pi/\Delta\tau$. The discrete imaginary time version of (S20), which is appropriate for comparison with our Matsubara frequency data, is

$$\Lambda_{{\rm fit},\Delta\tau}(\omega_n) = \sum_{j=1}^{N} \sum_{q=-\infty}^{\infty} \frac{A_j}{\left(\omega_n - \frac{2\pi q}{\Delta\tau}\right)^2 + \gamma_j|\omega_n - \frac{2\pi q}{\Delta\tau}| + \Omega_j^2}. \tag{S21}$$

The sum over q can be performed explicitly, using

$$\begin{aligned}\sum_{q=-\infty}^{\infty} \frac{1}{(x+q)^2 + A|x+q| + B^2} = &\frac{\psi\left(\frac{A}{2} + \frac{\sqrt{A^2-4B^2}}{2} + x\right) - \psi\left(\frac{A}{2} - \frac{\sqrt{A^2-4B^2}}{2} + x\right)}{\sqrt{A^2-4B^2}} \\ &+ \frac{\psi\left(1 + \frac{A}{2} + \frac{\sqrt{A^2-4B^2}}{2} - x\right) - \psi\left(1 + \frac{A}{2} - \frac{\sqrt{A^2-4B^2}}{2} - x\right)}{\sqrt{A^2-4B^2}},\end{aligned} \tag{S22}$$

where $\psi(x)$ is a polygamma function, $A = \frac{\gamma_j\Delta\tau}{2\pi}$, $B = \frac{\Omega_j\Delta\tau}{2\pi}$, and $x = \frac{\omega_n\Delta\tau}{2\pi}$ $(0 \le x < 1)$. This is the form we used in our fits to the QMC data.

C. Sources of error for transport measurements

Our numerical experiments entail several sources of error, particularly with respect to measurement of the DC resistivity via ρ_1 and ρ_2. In this appendix we first discuss error estimates for the finite size data shown in Fig. S5, and then estimate the error entailed by taking the largest available system to represent the thermodynamic limit.

ρ_2 is extracted directly from the value and second τ derivative of $\widetilde{\Lambda}(\tau)$ at $\tau = \beta/2$, which are in turn determined by a linear fit of $\widetilde{\Lambda}(\tau)$ vs $(\tau - \beta/2)^2$ over an appropriate window. The statistical errors on $\widetilde{\Lambda}(\tau)$ give rise to straightforward confidence intervals on $\widetilde{\Lambda}(\beta/2)$ and $\partial_\tau^2\widetilde{\Lambda}(\beta/2)$, which are propagated to yield the error estimates for ρ_2 reflected in Fig. S5.

Fig. S6 shows that statistical error is not a meaningful source of error for ρ_1. While the two component fit described in the text is consistently within a few percent of $\Lambda(\omega_n)$, the deviation substantially exceeds the statistical error bars on $\Lambda(\omega_n)$ in a systematic, frequency dependent way. It is beyond our simple approach to estimate the magnitude of the error in ρ_1 that this systematic deviation entails. An additional source of error is in numerical minimization–different starting guesses for the least squares

$$\alpha = 1.0, V = 1.0, \mu = 0.5, h = 4.6 \approx h_c$$

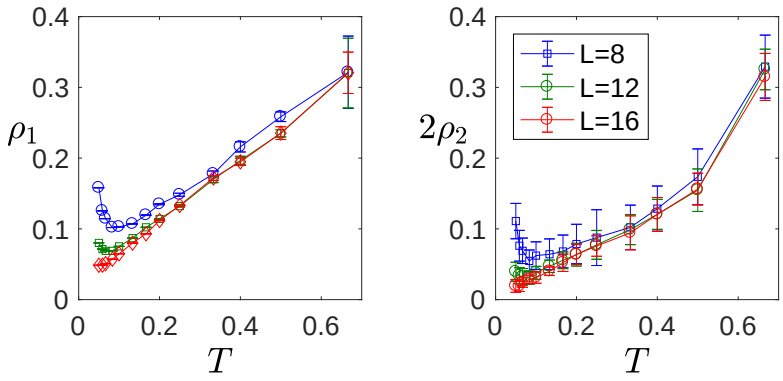

Figure S5. The temperature dependence of ρ_1 and ρ_2 for various system sizes, including error estimates.

$$\alpha = 1.0, V = 1.0, \mu = 0.5, h = 4.6 \approx h_c, \beta = 10, L = 16$$

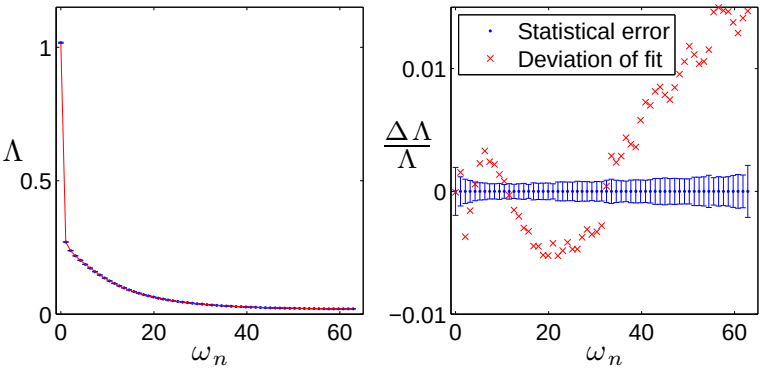

Figure S6. Left: data for $\Lambda(\omega_n)$ and the two-component fit described in the text. Right: the deviation between fit and data, expressed as a fraction of Λ, with statistical errors for comparison.

algorithm lead to variation of the inferred ρ_1 due to a broad minimum in the objective function, particularly at high temperature. This variation (for several choices of starting guess) yields the error bars pictured in Fig. S5.

For both ρ_1 and ρ_2, there are systematic finite-size errors that become increasingly important at low temperature. In the text, we quote the value for the largest system size simulated (between 16×16 and 20×20, depending on the temperature). To estimate the magnitude of the finite-size error, we perform a quadratic fit to the data as a function of $1/L$, as shown in Fig. S7. The difference between the $1/L \to 0$ extrapolation and the value for the largest system size is our estimate for the finite size error. The finite size error and the fitting/minimization error are added in quadrature to produce the

$$\alpha = 1.0, V = 1.0, \mu = 0.5, h = 4.6 \approx h_c, \beta = 10$$

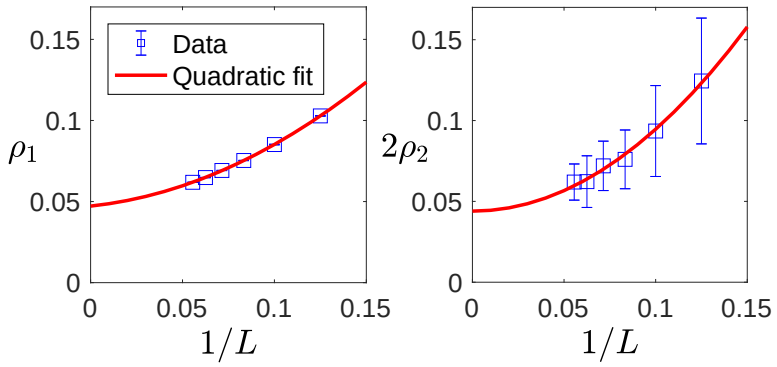

Figure S7. Estimation of finite size error via a quadratic fit in $1/L$.

error estimates in the paper. An identical procedure of error estimation is employed for the width and weight of the Drude-like piece shown in the paper.

D. Insensitivity of the fit to an additional narrow peak in $\sigma'(\omega)$

In the main text, we have used a simple two-component form for the conductivity $\sigma'(\omega)$ to fit the Matsubara frequency data. This is the "minimal" form that is required, in the sense that the data cannot be well described with a single component form. However, as we now show, we cannot exclude the presence of *additional* components. In particular, the data can be described equally well with an additional narrow peak in $\sigma'(\omega)$ centered at $\omega = 0$, whose width is much smaller than T.

In order to demonstrate this, we have repeated the fitting analysis describes in the paper with an additional delta-function contribution to $\sigma'(\omega)$ with a variable weight A. This corresponds to the following fitting function:

$$\tilde{\Lambda}_{\text{fit}} = \Lambda_{\text{fit}} + \pi A \delta_{\omega_n, 0}, \tag{S23}$$

where Λ_{fit} is the two component form used in the main text [Eq. (**??**) above]. In Fig. S8 we present the root mean square deviation of the best fit as a function of A. As seen in the figure, the fit quality improves slightly upon increasing A, until it reaches a certain critical value where the deviation turns up sharply. We conclude that our analysis of the conductivity cannot rule out the presence of additional "fine structure" of $\sigma'(\omega)$ at frequencies $\omega \lesssim T$. In particular, if such fine structure is present, the resistivity proxies can be dramatically different from the true DC resistivity. (For example, if $A \neq 0$, the DC resistivity is zero.)

Therefore, the resistivity proxies which we obtained by analyzing the imaginary time (or Matsubara frequency) correlator cannot be related to the true DC resistivity without further assumptions. The proxies can tell us about the DC resistivity only if $\sigma'(\omega)$ has a sufficiently simple structure at low

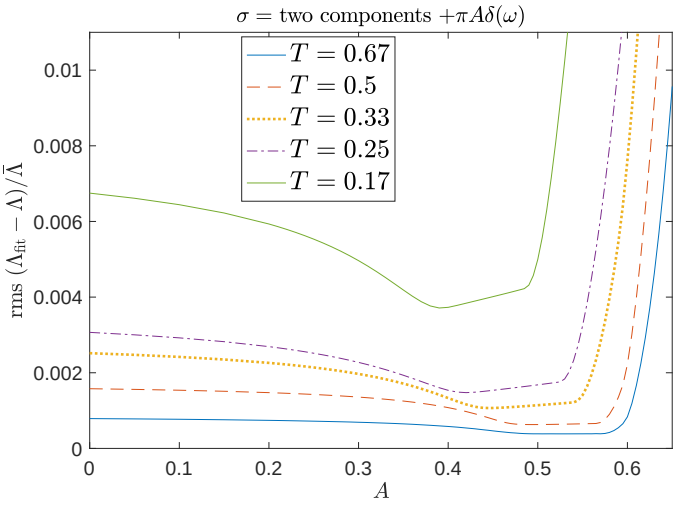

Figure S8. Softness of the two component conductivity fit to the addition of a sharp Drude peak. Plotted is the root mean squared deviation of the fit from the numerical data, normalized by $\bar{\Lambda}$, the mean value of Λ. The parameters used in the QMC run were $\alpha = 1.5$, $V = 0.5$, $\mu = 1$, $h = 2.6 \approx h_c$, and $L = 20$. The quality of the fit is modestly improved by the addition of a delta function component of fixed weight, with the remaining two components of form (**??**). As expected, we cannot rule out additional structure of the conductivity at frequencies far less than the temperature.

frequency, such as Eq. (S12) above. The appeal of this form is in its simplicity; however, there are well-defined scenarios where it might fail, e.g. due to the emergence of an approximate conserved momentum in the presence of a sharp Fermi surface. Whether this is the case in our problem requires going beyond the present analysis.

E. Comparison with maximal-entropy analytic continuation

As an additional test on our results, we obtain the conductivity by applying the maximal entropy method (maxEnt), using Bryan's algorithm [4, 5]. The maxEnt method, while not as constrained as the fitting approach we have used in the main text, is biased towards producing broad, featureless spectral functions. The resulting conductivity $\sigma(\omega)$, shown in Fig. S9 has two-peak structure much like the fitting function used in the main text. Close to criticality, the Drude-like peak at $\omega = 0$ has width comparable to T, and the resistivity roughly matches the results of the fit, $\rho_{\rm maxEnt} \approx \rho_2$. There is a greater discrepancy between the two component fit and the maximum entropy result far from h_c. This is consistent with the development of a parametrically sharp Drude peak (i.e. one with width much smaller than T), a feature likely to be ill-captured by any unbiased form of analytic continuation.

S-II. FERMION MASS ENHANCEMENT

We present evidence in the main text that the low temperature metallic states for h away from h_c are Fermi liquid-like in character, and should therefore be characterized by an effective quasiparticle

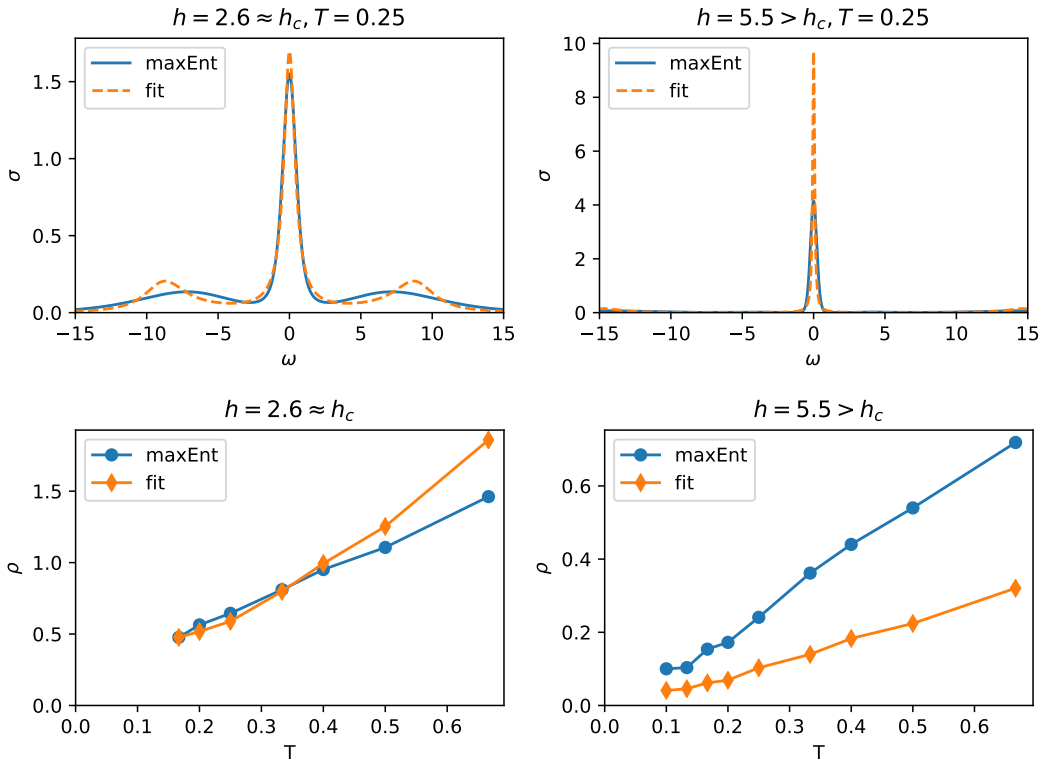

Figure S9. Top panels: The optical conductivity $\sigma(\omega)$ as obtained by maxEnt, compared with the fitting function shown in the main text. Bottom panels: The temperature dependence of the DC resistivity obtained by both methods. Shown here for $\alpha = 1.5, V = 0.5, \mu = 1$

dispersion. In this section we describe a method to approximately measure this dispersion near the Fermi surface, and show that it is subject to substantial flattening as $h \to h_c$. This reduction in the effective Fermi velocity, which is observed everywhere on the Fermi surface except the cold spots, is typically described as an enhanced effective mass.

We define a low-frequency moment of the spectral function, $\Omega_1\left(\vec{k}\right)$ from the Fermion green function $\widetilde{G}\left(\vec{k},\tau\right)$ according to

$$\Omega_1\left(\vec{k}\right) = -\partial_\tau \log\left[\widetilde{G}\left(\vec{k},\tau\right)\right]\Big|_{\tau=\beta/2} = \frac{\int d\omega \frac{\omega A\left(\vec{k},\omega\right)}{\cosh(\beta\omega/2)}}{\int d\omega \frac{A\left(\vec{k},\omega\right)}{\cosh(\beta\omega/2)}}, \tag{S24}$$

where the final equality is an exact identity. For a free fermion system, $\Omega_1\left(\vec{k}\right)$ precisely equals the dispersion. In a Fermi liquid at temperature T, there is a renormalized quasiparticle dispersion $\epsilon\left(\vec{k}\right)$, and as $\vec{k}$ approaches the Fermi surfaces, the spectral function is dominated by a peak centered at

$\epsilon\left(\vec{k}\right)$, with width much less than T. Accordingly, $\Omega_1\left(\vec{k}\right) \to \epsilon\left(\vec{k}\right)$ as $\epsilon\left(\vec{k}\right)/T \to 0$. Therefore, in a Fermi liquid, $\Omega_1\left(\vec{k}\right)$ is a valid proxy for the dispersion within a range $\sim T$ of the Fermi level. The assumptions above clearly break down close to criticality (at least away from the cold regions), where there are no well-defined quasiparticles.

In Fig. S10 we exhibit the momentum dependence of Ω_1 at fixed temperature for a variety of values of the tuning parameter h. Except for near the cold spots, Ω_1 tends to flatten near the Fermi level as h_c is approached. Similar results are found for smaller values of the coupling constant and the fermion density.

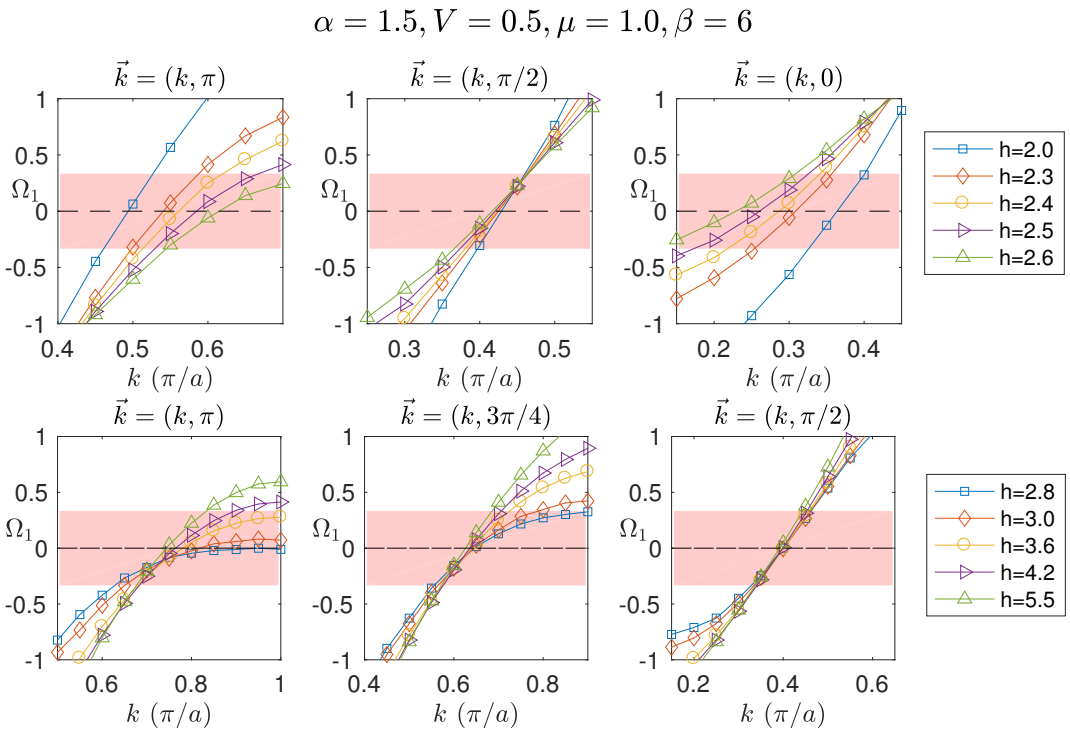

Figure S10. The low frequency moment Ω_1 along various cuts through the Fermi surface, showing mass enhancement on approach to the QCP. The QCP is located at $h \approx 2.6$, and for $h \leq h_c$ (upper row), a small symmetry breaking field has been applied to orient the nematic order so that hopping in the x direction is enhanced (this also cuts off fluctuation effects to some extent near h_c). The cut through $k_y = \pi/2$ passes near the cold spot, and has little mass enhancement on approach to the QCP. The shaded range is within $2T$ of the Fermi level, roughly where Ω_1 should faithfully measure the quasiparticle dispersion.

S-III. FERMION SPECTRAL FUNCTION

In this section we construct the fermionic spectral function $A_{\mathbf{k}}(\omega)$ by the maximum entropy method. Close to criticality, [Fig.S11], the spectral function away from the cold spots shows very broad features, without a well-defined dispersing peak. Below the superconducting T_c, a gap opens around $\omega = 0$.

At the cold spots or away from criticality [Fig.S12], we find well-defined peaks, showing a BCS-like transition into the superconducting phase. Although the maxEnt results are visually appealing and

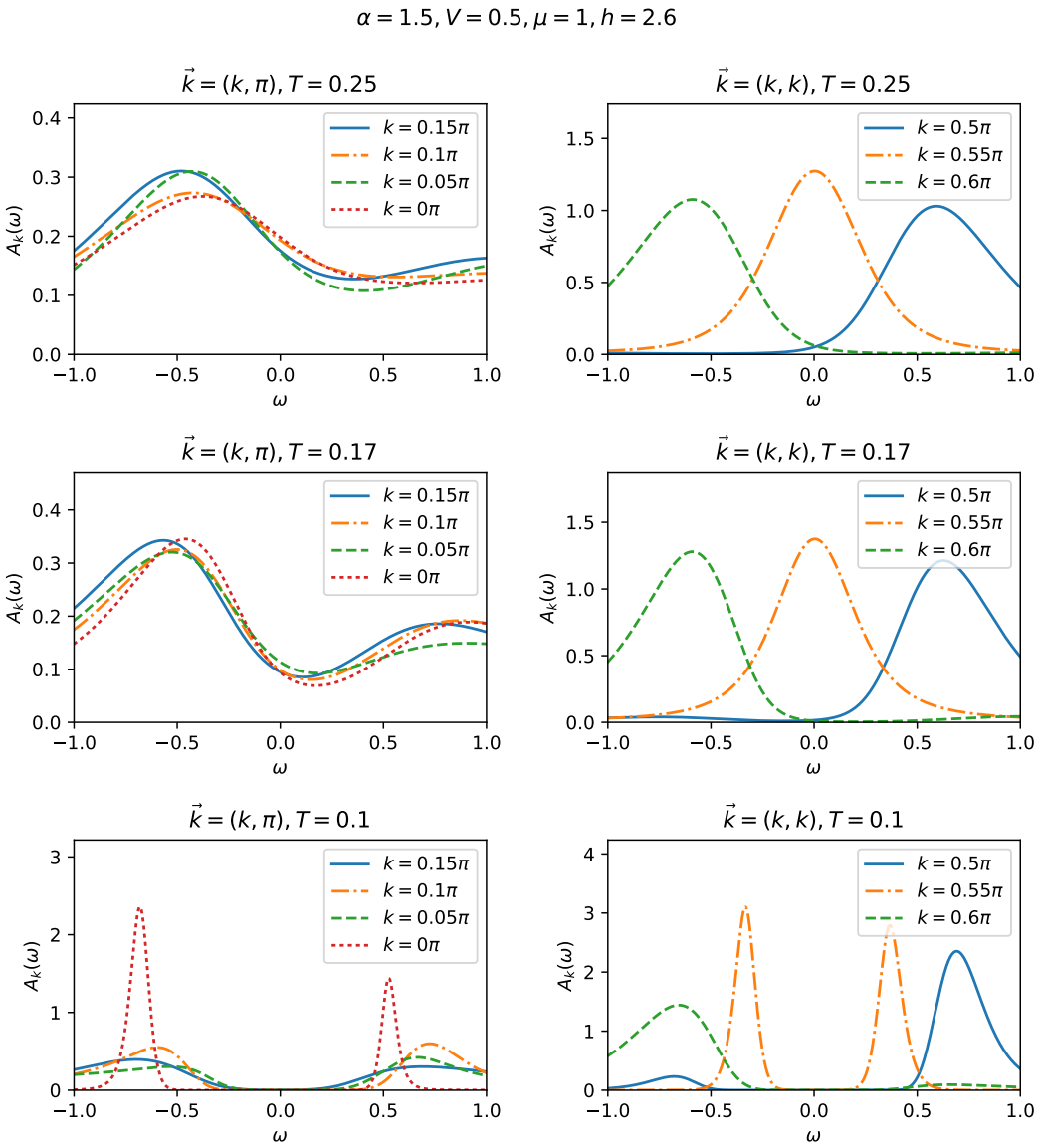

Figure S11. The fermionic spectral function as obtained by the maxEnt method. Different curves represent different momenta close to the Fermi surface. Shown here for $h \approx h_c$

agree with the direct analysis of imaginary-time data shown in the main text, a word of caution is in order. The maxEnt method favors spectral functions which are as smooth and featureless as possible, while still in agreement with the data. Thus, it is not reliable for extracting spectral features with

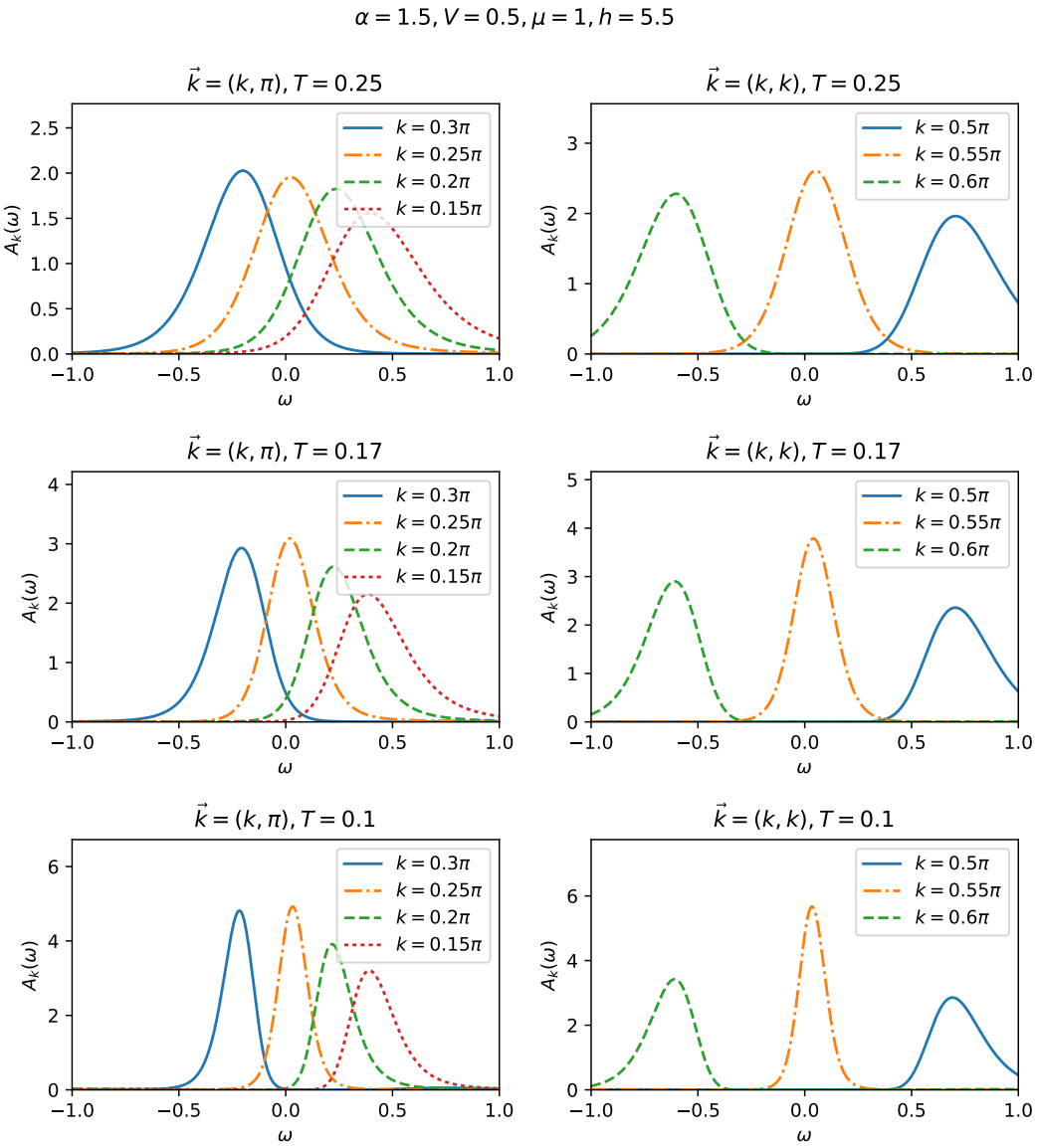

Figure S12. The fermionic spectral function as obtained by the maxEnt method. Different curves represent different momenta close to the Fermi surface. Shown here for $h > h_c$

typical frequencies much smaller than the temperature.

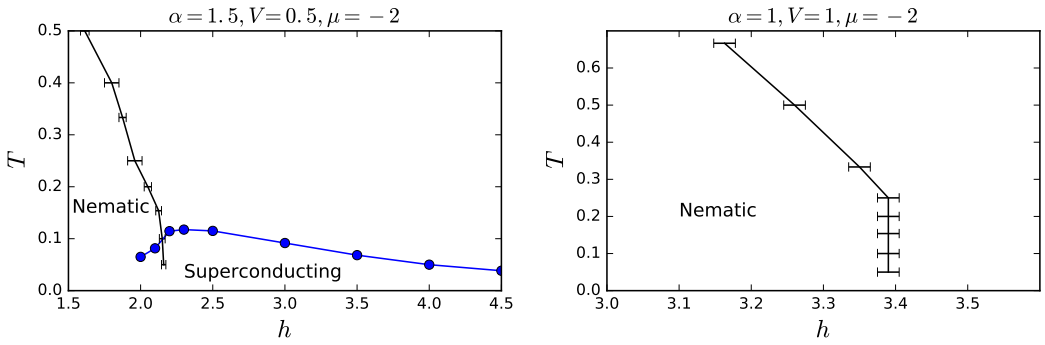

Figure S13. Phase diagrams for two values of the coupling constants.

S-IV. BEHAVIOR AT LOWER DENSITIES

In this section we present results for somewhat smaller densities than those presented in the main text. We focus on the two sets of couplings α and V as in the main text, with the chemical potential set to $\mu = -2$. In figure S13 we show the phase diagrams. For both couplings, the finite temperature nematic phase boundary $T_{\text{nematic}}(h)$ is linear at high temperature, and undergoes a sharp change of slope at lower temperatures. At the weaker coupling, $\alpha = 1$, a multi-peak structure is seen in the distribution of several thermodynamic quantities, such as the density and the nematic order parameter, suggesting a weakly first order transition at low temperatures. Whereas at the stronger coupling, $\alpha = 1.5$ and $V = 0.5$, we find a high T_c superconducting dome with maximal $T_c \approx 0.12$, there is no evidence of superconductivity for the weaker coupling, $\alpha = 1$ and $V = 1$, down to temperatures $T = 0.033$.

The imaginary part of the single fermion self-energy, shown in Fig. S14, shares similar characteristics to the larger-density data. A substantial "nodal-antinodal" dichotomy is seen, and the self energy close to $h = h_c$ seems to approach a constant as $\nu_n \to 0$. At the stronger coupling, $\alpha = 1.5$, the characteristic upturn of the self energy at low frequencies is seen below the superconducting T_c.

The estimates for the resistivity, ρ_1 and ρ_2, are shown in Fig. S15. As in the higher densities shown in the main text, the resistivity proxy ρ_2 (right column) agrees qualitatively with the results of the two-component fit ρ_1 (left column). The optical conductivity contains a Drude-like peak. The magnitude of the DC resistivity is of order of the quantum of resistance $\hbar/e^2$. However, unlike for higher densities, we do not find linear-in T resistivity over a range of temperatures close to the nematic quantum phase transition.

A possible cause for the qualitative difference in the resistivity between the lower and higher density systems is the smaller size of the Fermi surface at these densities, which might lead to a suppression of certain umklapp processes at low temperatures. For our Fermi surface, an umklapp scattering process involving two fermions near the Fermi point along the line $(0, \pi) - (\pi, \pi)$, $\vec{k}_h$, and symmetry-related points requires $k_h \geq \frac{\pi}{2}$. Similarly, a process involving two fermions near the Fermi points along the diagonal, $\vec{k}_d$, and symmetry-related points requires $k_d \geq \frac{\pi}{\sqrt{2}}$. The magnitudes of the Fermi momenta k_d and k_h, measured with respect to (π, π), are shown in Table I, and are found to be close to the aforementioned limiting values.

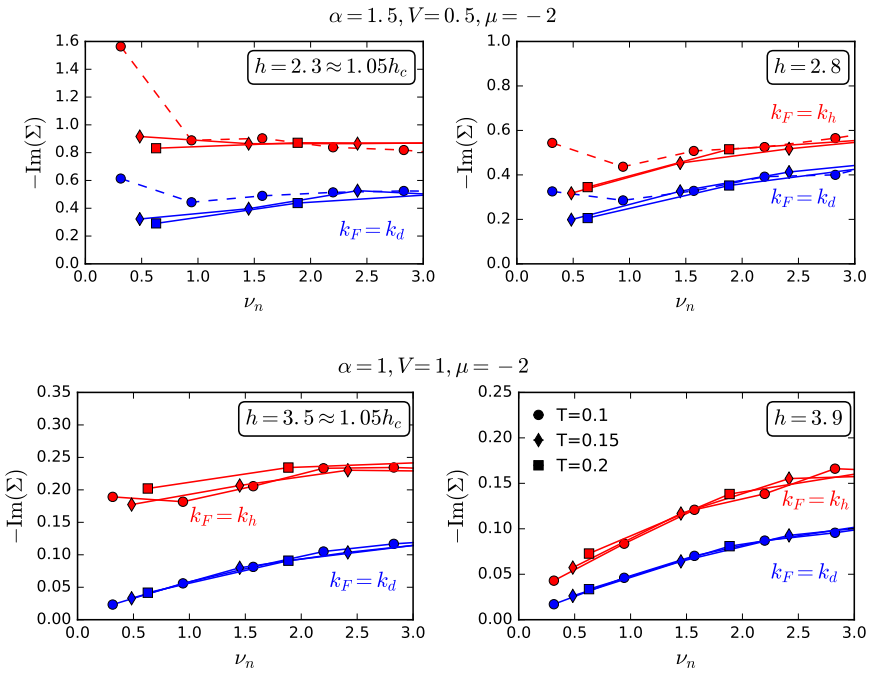

Figure S14. The imaginary part of the fermion self-energy, for various temperatures and with the nominal Fermi momenta k_d and k_h along the $(0,0)-(\pi,\pi)$ and $(0,\pi)-(\pi,\pi)$ directions, respectively. Data are shown for a 14×14 system both near h_c (left column) and somewhat in the symmetric phase (right column). In the upper panels, data points below T_c are connected by dashed lines.

	$\frac{2k_h}{\pi}$	$\frac{2k_d}{\sqrt{2}\pi}$
$\alpha = 1,\ V = 1,\ \mu = -2$	1.16 ± 0.08	0.72 ± 0.08
$\alpha = 1.5,\ V = 0.5,\ \mu = -2$	1.28 ± 0.08	0.80 ± 0.08

Table I. Magnitudes of Fermi momenta along high symmetry directions.

[1] Yoni Schattner, Samuel Lederer, Steven A. Kivelson, and Erez Berg, "Ising nematic quantum critical point in a metal: A monte carlo study," Phys. Rev. X **6**, 031028 (2016).

[2] Thereza Paiva, Raimundo R. dos Santos, R. T. Scalettar, and P. J. H. Denteneer, "Critical temperature for the two-dimensional attractive hubbard model," Phys. Rev. B **69**, 184501 (2004).

[3] Nandini Trivedi and Mohit Randeria, "Deviations from fermi-liquid behavior above T_c in 2d short coherence length superconductors," Phys. Rev. Lett. **75**, 312–315 (1995).

[4] Mark Jarrell and J.E. Gubernatis, "Bayesian inference and the analytic continuation of imaginary-time quantum monte carlo data," Physics Reports **269**, 133 – 195 (1996).

[5] R. K. Bryan, "Maximum entropy analysis of oversampled data problems," European Biophysics Journal **18**, 165–174 (1990).

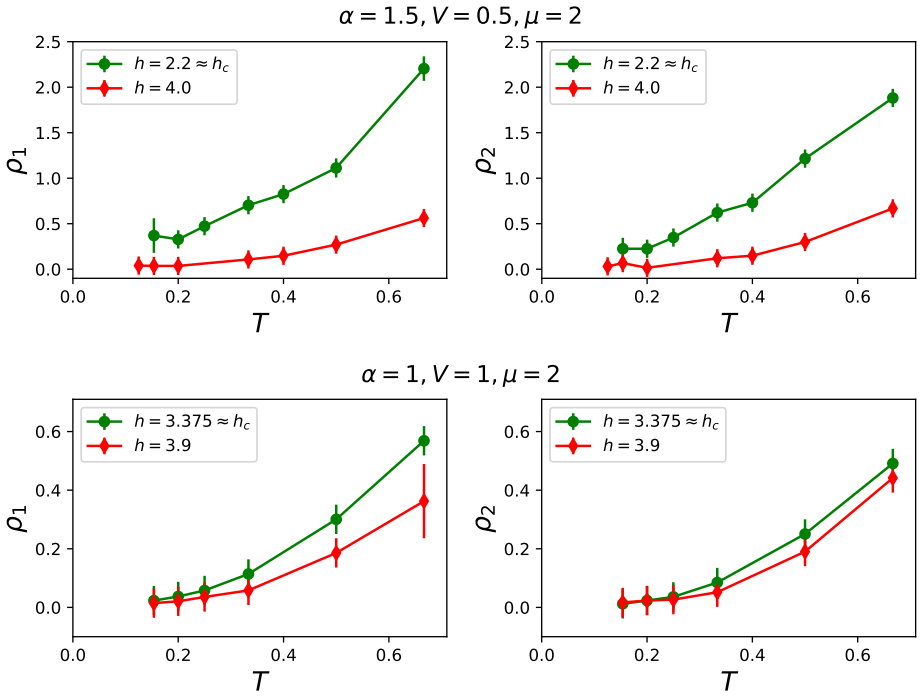

Figure S15. The temperature dependence of the resistivity proxies.